Light shadowing effect of large breast lesions imaged by optical tomography in reflection geometry

Chen Xu
Quing Zhu
University of Connecticut
Department of Electrical and Computer Engineering
371 Fairfield Road
Storrs, Connecticut 06269

Abstract. When a large, highly absorbing breast lesion is imaged by optical tomography in reflection geometry, most of the photons are absorbed by the top portion of the lesion. As a result, the lower portion of the lesion is not quantified correctly. This posterior light shadowing effect is similar to the sound shadowing effect frequently seen in pulse-echo ultrasound images. The presence of significant posterior shadowing of a lesion in ultrasound images suggests malignance. The light shadowing effect due to optical contrast is characterized using a simple measure and validated by the Monte Carlo photon-tracking method and phantom experiments. Clinical examples of large malignant and benign lesions are presented to demonstrate the shadowing effect and the utility of the measure. Understanding and quantifying the shadowing effect due to optical contrast is important for characterizing larger malignant cancers from benign lesions. © *2010 Society of Photo-Optical Instrumentation Engineers.* [DOI: 10.1117/1.3431086]

1 Introduction

Optical tomography using near-infrared (NIR) diffused light has shown great promise in distinguishing benign from malignant breast lesions and in assessing chemotherapy response of advanced breast cancers.[1–18] Three geometries have been used frequently in optical tomography: transmission geometry,[5–7] ring geometry,[17,18] and reflection geometry.[12–16] In reflection geometry, the measurements are typically made using a handheld probe with many source and detector fibers distributed on the probe. Compared with other imaging geometries, reflection geometry has the significant advantage of probing reduced breast tissue thickness. Therefore, lesions close to the chest wall can be imaged.

We have developed a co-registered ultrasound and optical tomography technique by deploying NIR source and detector fibers and a commercial ultrasound transducer on a handheld probe. Co-registered ultrasound is used to guide the NIR tomography for lesion localization and also for image reconstruction. Similar to the posterior shadowing effect of pulse-echo ultrasound when imaging larger tumors, we have frequently observed a significant posterior light shadowing effect when imaging these large tumors.[19] In other words, the reconstructed absorption maps of these large tumors have shown much higher light absorption at the top portion than that of the deeper portion. We have also seen heterogeneous light absorption distributions when imaging advanced cancers,[19] and we have systemically characterized and quantified the target heterogeneity in a recent study.[20] There are two dominant factors that contribute to the depth-dependent absorption mapping. The first is related to the weight matrix used for image reconstruction, and the second is due to significant light absorption of a tumor that causes a dramatic reduction of the reflected light received from the deeper portion of the tumor.

In our image reconstruction, Born approximation was used to relate the unknown optical properties of the tissue to the measurements at the surface, and inversion was performed with the conjugate gradient iterative searching method. A semi-infinite absorbing boundary condition was used to derive the weight matrix that had the so-called banana shape for a given source and detector pair. This "banana function" causes the reconstructed optical properties to be depth dependent because the iterative searching method is highly prone to converge along the steepest direction—i.e., the largest weight direction. As a result, even for a homogeneous large target, the reconstructed absorption coefficients of top target layers, which normally have more weight, are higher than those of the deeper target layers, which normally have less weight.[21] This is an intrinsic problem related to light diffusion in the turbid medium and can be partially corrected by appropriately scaling the weight matrix.[21] The second contributing factor to the depth-dependent absorption mapping is due to the significant light absorption of a highly vascularized tumor, which causes a dramatic reduction of the reflected light received from the deeper portion of the tumor.

In this paper, we have derived a simple measure to evaluate the posterior light shadowing caused by optical absorption of large targets. This simple measure is independent of target location and, instead, depends on optical contrast of the target

Address all correspondence to: Quing Zhu, University of Connecticut, Department of Electrical and Computer Engineering, 371 Fairfield Road, Storrs, Connecticut 06269. Tel: 860-486-5523; Fax: 860-486-2447; E-mail: zhu@engr.uconn.edu

of different size. The objective is to characterize large malignant cancers from benign lesions based on optical contrast only.

The Monte Carlo (MC) photon-tracking method has been developed to systemically evaluate the relationship between the light shadowing effect and the target optical contrast. Phantom experiments are performed to validate the simulation results, and clinical examples are given to demonstrate the light shadowing effect and the utility of the measure. To the best of our knowledge, the light shadowing effect due to optical contrast has not been reported and characterized in the literature. Understanding and quantifying this effect is an important step toward translating the optical tomography technique, especially when implemented in reflection geometry, into clinics for breast cancer diagnosis.

2 Methods

2.1 Monte Carlo Simulation

The MC method[22] was adopted to simulate the light propagation in a scattering medium and to visualize the absorption distribution inside the medium. Briefly, the turbid medium was modeled as having layers with finite thickness (along the depth, z axis) of specified optical properties in each layer. If the medium is homogeneous, all layers will have the same optical properties. In the simulation, millions of photons were generated at each source location. Each photon was incident at 90 deg to the surface of the turbid medium and was assigned a unity weight $\mathbf{W}$, which is analogous to the light intensity. Each photon went through many steps of absorption and scattering processes. After each step, part of the weight ΔW was absorbed by the medium, and the weight of the photon was decreased. The photon was scattered following the Henyey-Greenstein function. The medium anisotropy, g, was chosen to be 0.9 in this simulation. The roulette technique was used to terminate the photon when $W \leqslant W_{th}$, where W_{th} was a threshold value. Each photon either was absorbed in the medium, was detected at the reflecting surface, or exited the transmitting surface. After the migration of one particular photon halted, a new photon was launched into the medium at the source location. The MC simulation was performed in the time domain,[23] and the resulting temporal data were Fourier transformed to provide frequency-domain amplitude and phase shift as a function of distance. In this simulation, the boundary condition can easily be controlled through the use of refractive indices of the surface layer and the medium layer.[24] The absorption boundary was used between the scattering medium and the outer surface. The photon energy was recorded when it reached the outer surface (boundary) without further reflection.

The MC program was extended to include a spherical target embedded inside the medium. The size, position, and optical properties of the target were controlled from an input file. The complex photon reflection and refraction at the interfaces of the target and the medium were computed. It is important to decide whether a photon was reflected or refracted at the interface between the target and the medium. The angle of incidence, the angle of reflection, and the angle of refraction were calculated in three dimensions. As shown in Fig. 1, a plane P was established based on three points: center of the target (O), the original position of the photon (E), and the
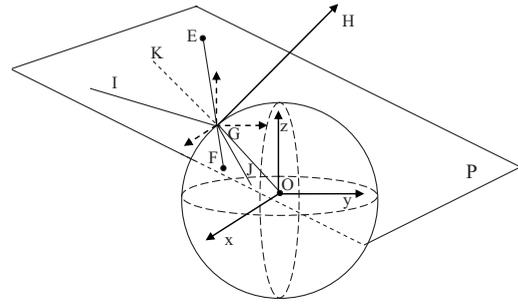

Fig. 1 Illustration of the MC simulation when a target is embedded in the medium.

expected position of the photon after one-step propagation (F), assuming no reflection/refraction. The interception of the photon propagation direction with the target is G. Plane P can be expressed as

$$\cos(A)x + \cos(B)y + \cos(C)z - p = 0, \quad (1)$$

where A, B, and C were azimuthal angles of the normal vector (GH) for plane P, and p was the distance from the plane P to the center of the coordinate in the normal direction. Snell's law was applied to calculate the reflection angle ($\angle KGI$) and refraction angle ($\angle OGJ$) in plane P. The calculated reflection or refraction angle was converted to the azimuthal angle in the original (x, y, z) coordinates by solving the following equation:

$$\cos^2 \varphi \cdot \sin^2 \beta - 2\sin \gamma \sin^2 \beta \sqrt{\sin^2 \beta - \cos^2 \alpha} \cdot \cos \varphi$$
$$+ \sin^2 \beta(\sin^2 \gamma \sin^2 \beta - \cos^2 a) = 0, \quad (2)$$

where φ was one azimuthal angle of the reflection/refraction line, α was the corresponding azimuthal angle of incident line, β was the corresponding azimuthal angle of normal line of plane P, and γ was the angle between the incident line and reflection line.

If a photon experienced total internal reflection, the photon was first propagated to the point where its trajectory intersected the boundary between the target and the medium via a shortened step size (s_1). Then, the photon's traveling direction was changed to the reflection direction and propagated the remaining step ($s - s_1$) in the same medium. If the photon experienced partial internal reflection, we simplify the computation by assuming that the photon was either all reflected or all refracted. To determine that, the reflection coefficient from Fresnel's equations[25] was computed and compared with a random number generated from a uniform distribution. If the random number was less than the reflection coefficient, the photon experienced reflection; otherwise, it was refracted. In the latter case, the photon propagated to the boundary first and then continued by following the refraction direction. The final spatial location of the photon was calculated by propagating the photon with a distance of $s - s_1$, which was adjusted in length according to the difference in total interaction coefficients between the medium and the target. The total interaction coefficient is the summation of the absorption coefficient and the scattering coefficient.
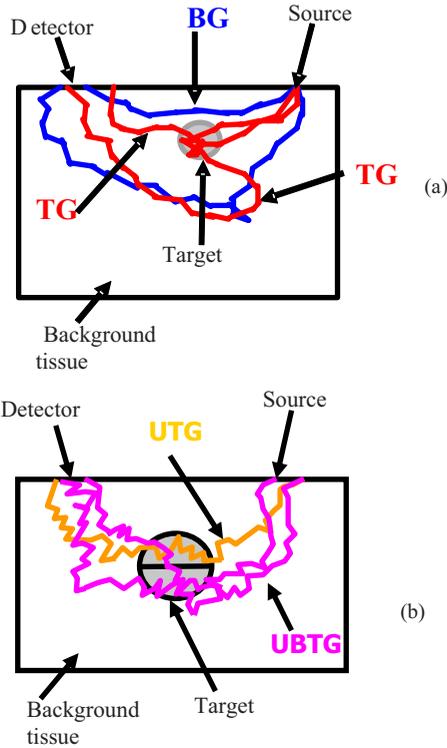
Fig. 2 Illustration of different photon groups. (a) Illustration of photon groups when a single target is embedded in the medium. Target group (TG) consists of photons that enter the target; background group (BG) consists of photons that propagate in the background medium only. (b) Illustration of photon groups when the target is segmented into top and bottom layers. Upper target group (UTG) consists of photons that enter the upper half target only; upper and bottom target group (UBTG) consists of photons that enter both the upper and bottom parts of the target.

2.2 Photon Tracking Method

The MC method has the advantage of tracking each generated photon.[26] The detected photon can be separated into several groups according to the propagation path of the photon. To compute the contributions of each target or top portion or bottom portion of the target to the measured reflectance, we categorize each received photon at the surface into different groups. The first group consists of photons that do not enter the target (BG), and the second group consists of photons that enter the target (TG). Figure 2(a) illustrates example paths of these two photon groups. The TG group can be further categorized into many subgroups based on the deepest depth that each photon has reached. For example, as shown in Fig. 2(b), if the target is separated into the upper half and the bottom half, the photons that entered the target can be further categorized into two subgroups: the photons entering the upper half target only (UTG) and the photons reaching the bottom half (UBTG). By summing the weights of detected photons from each group and then dividing the total weight, we obtained the intensity ratio as

$$P_i(s,d) = W_i/W_t \quad i = 1, 2, \qquad (3)$$

where $W_i = \Sigma_l W_{il}$, l is the index of received photons of each group. $W_t = \Sigma_{i=1}^{n} W_i$ is the total weight. n is the total number of

groups. The ratios of different groups provide information that is group specific at each detector location (d) for a specified source location (s). The ratio between subgroups can also be calculated, such as the ratio between the intensity of photons entering the upper-half UTG and the intensity of photons reaching the bottom-half UBTG. This ratio is denoted as $P(s,d) = (W_{UTG}/W_t)/(W_{UBTG}/W_t) = W_{UTG}/W_{UBTG}$ in the following text, and it corresponds to the received scattered wave from the top part of the target to the bottom part of the target.

2.3 Weight Matrix Calculation and Image Reconstruction

The Born approximation is used to relate the scattered field $U_{sd}(r_{si}, r_{di})$ measured at the source (s) and detector (d) pair i to absorption variations $\Delta\mu_a(r')$ in each volume element r' within the sample. A dual-zone mesh scheme introduced by us earlier[12] was used to segment the imaging volume into lesion region (L) and background region (B) with finer and coarse voxel sizes, respectively. This scheme significantly reduced the total number of voxels with unknown optical properties and improved the convergence. In general, the inversion converged in three to four iterations. The measured scattered field, weight matrix, and total absorption distributions were related in the following equation as

$$[U_{sd}]_{M \times 1} = [W_L, W_B]_{M \times N}[M_L, M_B]^T, \qquad (4)$$

where $W_L = [-G(r_{vj}, r_{di})\Phi_0(r_{si}, r_{vj})/D]_{M \times N_L}$ and $W_B = [-G(r_{vk}, r_{di})\Phi_0(r_{si}, r_{vk})/D]_{M \times N_B}$ were weight matrices for lesion and background volumes, respectively, and $[M_L] = [\int_{1_L} \Delta\mu_a(r')d^3r', \ldots \int_{N_L} \Delta\mu_a(r')d^3r']$ and $[M_B] = [\int_{1_B} \Delta\mu_a(r')d^3r', \ldots \ldots \int_{N_B} \Delta\mu_a(r')d^3r']$ were the total absorption distributions of lesion and background volumes, respectively. G was the Green's function, Φ_0 was the incident field, and D was the diffusion constant. Instead of using a traditional inversion approach that reconstructs the $\Delta\mu_a(r')$ directly, we have reconstructed the total absorption distribution. The total is divided by the different voxel sizes of the lesion and background at the end of the iterative optimization to obtain the absorption distribution $\Delta\mu_a(r')$. This scheme further conditions the inversion and improves the convergence because the total absorption distribution in the background region with a lower $\Delta\mu_a$ and a larger voxel size has the similar scale as the total in the lesion region with a higher $\Delta\mu_a$ and a smaller voxel size. Furthermore, dividing the voxel size at the end of the iterative inversion has significantly reduced background artifacts because the voxel size in the background region was much larger than that at the lesion region. The conjugate gradient method was used for the optimization.

The scattered wave or perturbation received at the surface due to the presence of an absorbing target can be approximated as $U_{sd} = U_{top} + U_{bottom} + U_{background}$, where U_{top} and U_{bottom} represent the perturbation generated from the top part and bottom part of the target, respectively, and $U_{background}$ is from the background. The reconstructed total absorption distribution has three components of $\Delta\mu_{a\_top}$, $\Delta\mu_{a\_bottom}$, and $\Delta\mu_{a\_background}$ if the medium scattering heterogeneities are neglected. We then have the following equation derived from Eq. (4) as

$$(U_{top} + U_{bottom} + U_{background}) = (W_{L\_top} \times \Delta\mu_{a\_top} + W_{L\_bottom}$$
$$\times \Delta\mu_{a\_bottom} + W_B$$
$$\times \Delta\mu_{a\_background}). \quad (5)$$

Assuming that the background perturbation, $\Delta\mu_{a\_background}$, is negligible compared with that of the target, we reach the following approximation:

$$U_{top} \approx W_{L\_top} \times \Delta\mu_{a\_top} \text{ and} \quad (6)$$

$$U_{bottom} \approx W_{L\_bottom} \times \Delta\mu_{a\_bottom}.$$

We further assume the simplest case, that the reconstructed target absorption distribution is uniform for top and bottom portion of the target with constant values $\Delta\mu_{a\_top}$ and $\Delta\mu_{a\_bottom}$. The ratio of U_{top} to U_{bottom} is directly related to $\Delta\mu_{a\_top}$ and $\Delta\mu_{a\_bottom}$ as

$$R(s,d) = \frac{|U_{top}|}{|U_{bottom}|} = \frac{\left|\sum W_{L\_top} \times \Delta\mu_{a\_top}\right|}{\left|\sum W_{L\_bottom} \times \Delta\mu_{a\_bottom}\right|},$$

$$= \frac{\left|\sum_{V\_top} W_{L\_top}\right| \times \Delta\mu_{a\_top}}{\left|\sum_{V\_bottom} W_{L\_bottom}\right| \times \Delta\mu_{a\_bottom}}$$

$$= \frac{\left|\sum_{V\_top} -G(r_{vj},r_d)\Phi_0(r_s,r_{vj})/D\right| \times \Delta\mu_{a\_top}}{\left|\sum_{V\_bottom} -G(r_{vj},r_d)\Phi_0(r_s,r_{vj})/D\right| \times \Delta\mu_{a\_bottom}},$$

$$= \kappa(s,d,\bar{\mu}_a,\overline{\mu_s'},location,volume)\frac{\Delta\mu_{a\_top}}{\Delta\mu_{a\_bottom}}, \quad (7)$$

where || represents the absolute value. κ is the ratio of the summation of two weight matrices computed from the top portion of the target and the bottom portion of the target. κ is a function of source and detector positions, background absorption and scattering coefficients, and target location and volume. κ characterizes the weighting of the photons propagating through the top portion of the target over the bottom portion of the target and is independent of the target contrast. Because both incident field Φ_0 and Green's function G exponentially decay with the depth, the summation of the weight computed from the top portion of the target is larger than that computed from the bottom portion of the target. The ratio κ increases with the target volume and target depth.

2.4 Quantifying Light Shadowing Effect Due to Target Optical Contrast Only

Based on the perturbation approach, the $R(s,d)$ is quantitatively related to the $P(s,d) = W_{UTG}/W_{UBTG}$ in the MC simulation, which is the intensity ratio of the received photons entering the upper-half target only, UTG, and photons reaching the bottom-half target, UBTG. For each pair of high-contrast and low-contrast targets of the same size located at the same depth, $R_{high}(s,d)$ and $R_{low}(s,d)$ can be calculated.

The ratio of $R_{high}(s,d)$ and $R_{low}(s,d)$ given in the following equation cancels the weighting effect due to $\kappa(s,d,\bar{\mu}_a,\overline{\mu_s'},location,volume)$ and characterizes the light shadowing effect due to target contrast only:

$$R_{high/low} = \frac{R_{high}(s,d)}{R_{low}(s,d)} = \frac{\left.\dfrac{\Delta\mu_{a\_top}}{\Delta\mu_{a\_bottom}}\right|_{high}}{\left.\dfrac{\Delta\mu_{a\_top}}{\Delta\mu_{a\_bottom}}\right|_{low}}. \quad (8)$$

Similarly, the ratio computed from high-contrast target $P(s,d)_{high} = W_{UTG}/W_{UBTG}$ and low-contrast target $P(s,d)_{low} = W_{UTG}/W_{UBTG}$ also cancels the weighting effect and depends on target contrast only.

The estimation derived earlier attempts to explain the approximate relationship between $(\Delta\mu_{a\_top})/(\Delta\mu_{a\_bottom})$ measured from absorption maps and intensity ratio $P(s,d) = W_{UTG}/W_{UBTG}$ computed from the MC simulations. In experiments, it is impossible to separate the perturbation measurements into contributions from top and bottom parts of the target. However, the reconstructed $\Delta\mu_{a\_top}$ and $\Delta\mu_{a\_bottom}$ can be measured from absorption images and can be quantitatively related to average percentage of weight $P = W_{UTG}/W_{UBTG}$. In the computation, the maximum μ_as measured at the top and bottom parts of the target were used to approximate the $(\Delta\mu_{a\_top})/(\Delta\mu_{a\_bottom})$ as $(\max \mu_{a\_top})/(\max \mu_{a\_bottom})$. This approximation avoids the computation problem when the $\Delta\mu_{a\_bottom}$ is too small.

2.5 Phantom and Clinical Experiments

The experimental validation was performed using our existing frequency domain NIR system.[27] It consisted of laser diodes of 780-nm and 830-nm wavelengths. The outputs of the laser diodes were amplitude modulated at 140 MHz and optically switched to 9 positions on a handheld probe. Fourteen optical fibers of 3-mm diameter were coupled to 14 parallel detection channels. For phantom experiments, Intralipid solution was used to emulate background breast tissue optical properties. Polyester resin spheres of calibrated values $\mu_a = 0.23$ cm^{-1} and $\mu_s' = 5.45$ cm^{-1}, and $\mu_a = 0.07$ cm^{-1} and $\mu_s' = 5.50$ cm^{-1} were used to emulate high-contrast tumors and low-contrast benign lesions. Both high- and low-contrast targets have three sizes of 1.0-, 2.0-, and 3.0-cm diameter to emulate small, medium, and larger lesions. In each experiment, the measurements were first made from a simple Intralipid background that was used as the reference data. The measurements were repeated for selected solid target phantoms immersed in the Intralipid background at known depths. A commercial ultrasound probe was located in the middle of the handheld probe to provide the depth and the location of the target.

The same setup has been used for clinical studies. The study protocol was approved by the local Institution Review Board. Signed informed consent was obtained from all patients who agreed to participate in the study. Patients were scanned in a supine position while multiple sets of optical reflectance measurements were made with co-registered ultrasound images at the lesion location and the normal contralateral location of the same quadrant as the lesion. The measure-
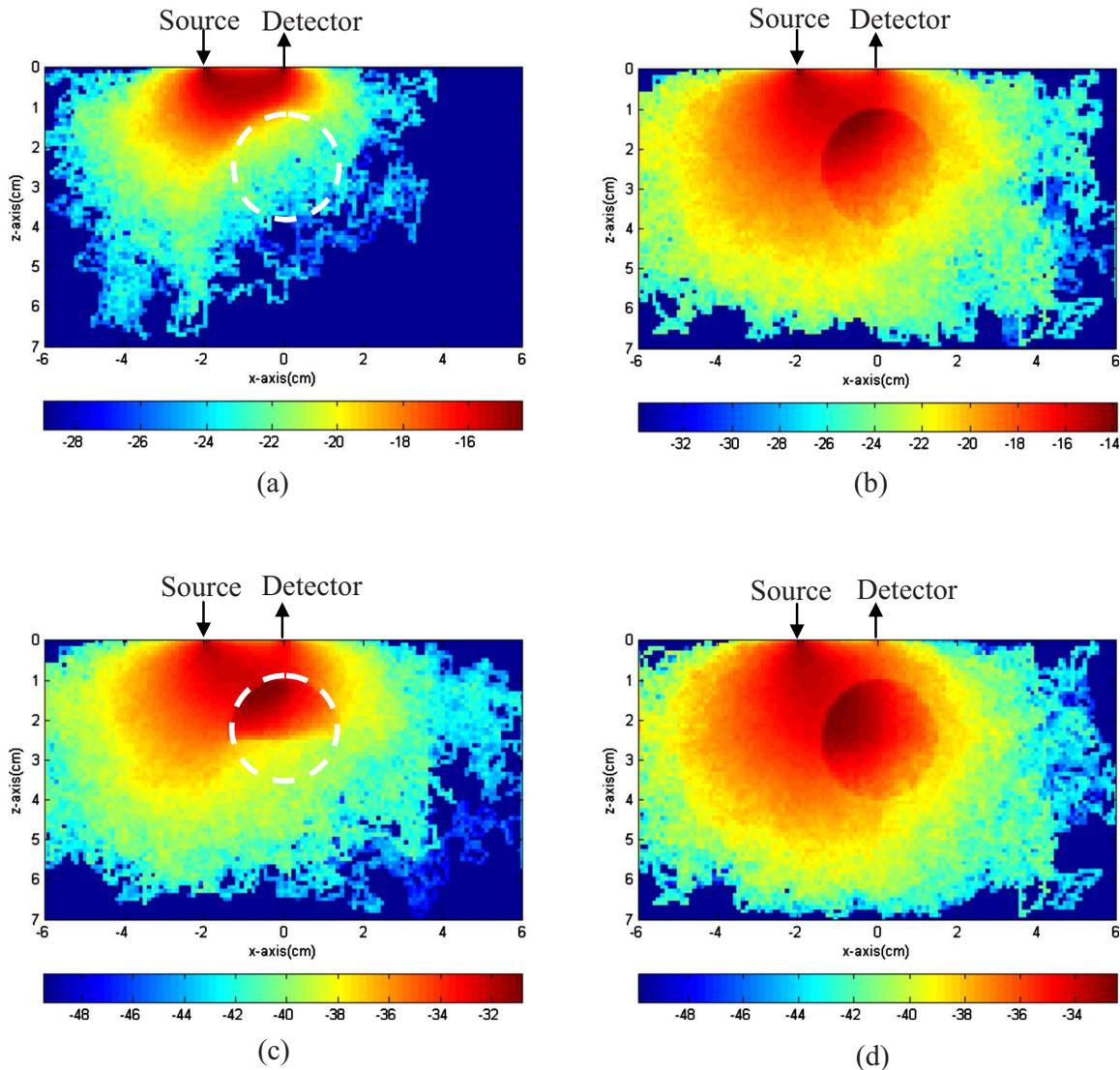
Fig. 3 Simulated absorbed weight distribution of a single target inside the 3-D volume was summed in the y direction and projected to the x-z plane. (a) The background photon group (BG) consists of photons that do not enter the target. (b) The target group (TG) consists of photons that enter the target. (c) The upper target group (UTG) includes the photons entering the upper half target only, when the target is separated into the upper half and the bottom half. (d) The upper and bottom target group (UBTG) includes the photons that reach the bottom half target when the target is separated into two parts.

ments obtained at the normal location were used to estimate background optical properties, which were used to compute the weight matrix for imaging.

3 Results

3.1 Example of Absorption Distributions of Different Photon Groups

In the first set of MC simulations, photons have propagated in a 12 cm × 12 cm × 7.5 cm volume of background μ_a =0.03 cm^{-1} and μ_s' =6.0 cm^{-1}. A simulated lesion of 3-cm diameter and μ_a =0.3 cm^{-1} and μ_s' =6.0 cm^{-1} was located at $(0,0,2.5$ cm$)$. The simulated lesion has the same refractive index of n =1.33 as that of the background medium. The source was located at $(-2.0,0,0$ cm$)$, and the detector was located at $(0,0,0$ cm$)$. In MC simulation, each photon was assigned an initial weight of unity. As the photon propagated in the medium, part of the weight ΔW was absorbed after each step. The absorbed ΔW inside the 3-D volume was summed in the y direction and projected into the x-z plane, as shown in Fig. 3. In each figure, the vertical axis is the propagation depth z in centimeters, and the horizontal axis is the lateral dimension x in centimeters. Each figure is normalized to the total number of photons and displayed in logarithmic scale. The target position is marked with a white dashed circle. Figures 3(a) and 3(b) show absorption distributions of the photons that have propagated in the background medium only (BG group) and entered the target (TG group), respectively. Figure 3(c) is the distribution of the photons that have entered the upper part of the target only (UTG group), and Fig. 3(d) is the distribution of photons that have entered both the upper and bottom parts of the target (UBTG group).
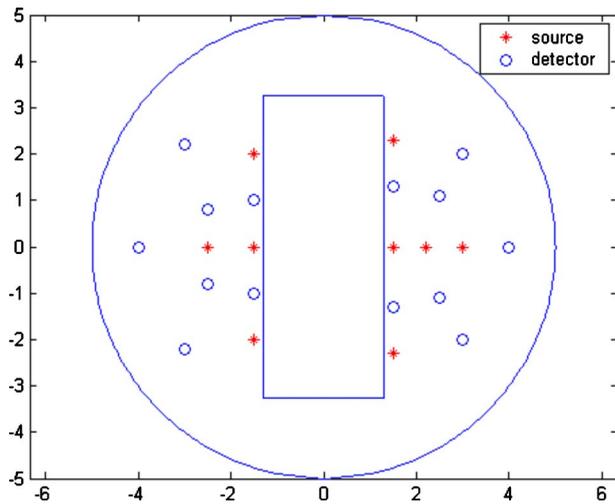
Fig. 4 Probe geometry used for simulation and phantom experiments. The red stars are the locations of sources, and the blue circles are the locations of detectors. The middle slot is used for a commercial ultrasound transducer. (Color online only.)

3.2 *Computed Intensity Ratios of Two-Photon Groups*

The MC simulations were performed for small, medium, and large spherical targets of 1.0-, 2.0-, and 3.0-cm diameters located at different depths, respectively. The background optical properties were $\mu_a = 0.03$ cm^{-1}, $\mu_s' = 6.0$ cm^{-1}, and the target optical properties were $\mu_a = 0.3$ cm^{-1}, $\mu_s' = 6.0$ cm^{-1} for the high-contrast case and $\mu_a = 0.1$ cm^{-1}, $\mu_s' = 6.0$ cm^{-1} for the low-contrast case. All targets were located at $(0, 0, z)$ cm, and center depth, z, was varied from 1.0 to 3.0 cm. Figure 4 is the imaging probe with the source and detector positions marked. Using this probe, the intensity ratio ($P = W_{UTG}/W_{UBTG}$) was calculated for both high- and low-contrast targets at all source–detector pairs. The average $P = W_{UTG}/W_{UBTG}$ was 3.04, 4.34, and 6.62 for the high-contrast 3-cm target located at 2.0, 2.5, and 3.0 cm, respectively; and the corresponding P was 1.86, 2.68, and 4.06 for the low-contrast target of the same size. The intensity ratios under other imaging conditions are given in Table 1. As predicted by Eq. (7), $P = W_{UTG}/W_{UBTG}$ increases with the target depth. However, the ratio of P_{high}/P_{low} according to Eq. (8) is independent of the source–detector separation and the target location and dependent on target contrast only when the target

Table 1 Simulation results for high-contrast targets and low-contrast targets at different center depths.

		Center Depth (cm)							
Target Diameter (cm)		1.5 cm		2.0 cm		2.5 cm		3.0 cm	
		High-Contrast Target	Low-Contrast Target	High-Contrast Target	Low-Contrast Target	High-Contrast Target	Low-Contrast Target	High-Contrast Target	Low-Contrast Target
$D = 1.0$ cm	Mean intensity ratio (W_{UTG}/W_{UBTG})	0.62	0.51	0.84	0.68	1.21	0.92	1.11	0.93
	Reconstructed max μ_a (cm^{-1}) [max in top layer; max in bottom layer]	[0.166 0.233]	[0.141 0.155]	[0.218 0.188]	[0.148 0.132]	[0.245 0.206]	[0.135 0.127]	[0.221 0.160]	[0.133 0.125]
	Reconstructed ratio R_{high} or R_{low}	0.71	0.91	1.16	1.13	1.19	1.06	1.38	1.06
$D = 2.0$ cm	Mean intensity ratio (W_{UTG}/W_{UBTG})	0.84	0.65	1.51	1.15	2.30	1.56	3.27	2.15
	Reconstructed max μ_a (cm^{-1}) [max in top layer; max in bottom layer]	[0.095 0.066]	[0.062 0.046]	[0.104 0.068]	[0.074 0.058]	[0.115 0.056]	[0.077 0.056]	[0.190 0.066]	[0.081 0.045]
	Reconstructed ratio R_{high} or R_{low}	1.45	1.36	1.54	1.28	2.05	1.37	2.87	1.77
$D = 3.0$ cm	Mean intensity ratio (W_{UTG}/W_{UBTG})			3.04	1.86	4.34	2.68	6.62	4.06
	Reconstructed max μ_a (cm^{-1}) [max in top layer; max in bottom layer]			[0.109 0.033]	[0.080 0.039]	[0.127 0.030]	[0.106 0.042]	[0.152 0.030]	[0.103 0.033]
	Reconstructed ratio R_{high} or R_{low}			3.30	2.08	4.23	2.52	5.08	3.13

Table 2 Simulation results for the ratio P_{high}/P_{low} when a pair of high- and low-contrast targets located at different center depths.

| Target Diameter (cm) | | Center Depth (cm) | | | |
		1.5 cm	2.0 cm	2.5 cm	3.0 cm
$D=1.0$ cm	Slope	0.0157	0.0232	−0.0844	0.0120
	Mean	1.0423	1.1428	1.1645	1.1691
	Standard deviation	0.5423	0.6321	0.7716	0.8345
$D=2.0$ cm	Slope	−0.0215	−0.0195	−0.0122	−0.040
	Mean	1.2781	1.3382	1.3895	1.4533
	Standard deviation	0.5700	0.5676	0.6868	0.6759
$D=3.0$ cm	Slope		−0.0857	0.0191	−0.0572
	Mean		1.6207	1.6474	1.6497
	Standard deviation		0.6577	0.8587	0.8234

size is the same. As shown in Table 2, the average values of P_{high}/P_{low} were 1.62, 1.65, and 1.65 when the center of the high- and low-contrast targets was located at 2.0, 2.5, and 3.0 cm, respectively. The average is fairly constant and independent of depth. This indicates that the ratio of the total number of received photons from the top portion of the target to the bottom portion of the target is 1.6 higher for the high-contrast target compared with that of the low-contrast target of the same size. In other words, the high-contrast target experiences 1.6 times higher light shadowing effect independent of the target location.

A similar comparison can be made for the medium-size and small-size targets. Figure 5 shows an example of
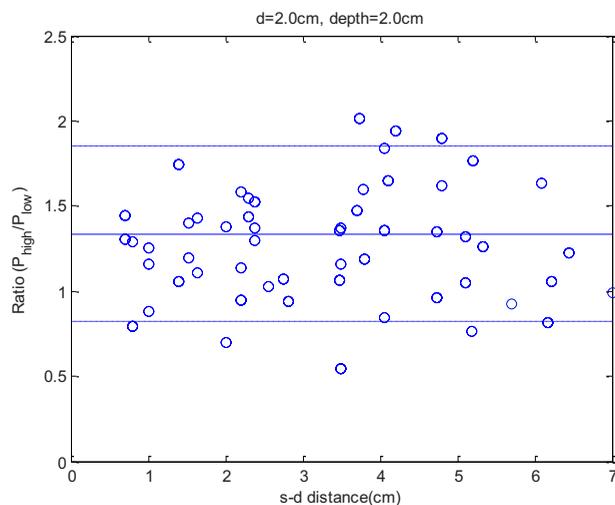

Fig. 5 An example of ratio P_{high}/P_{low} versus source–detector separation. The x axis is the source–detector distance, and the y axis is the P_{high}/P_{low}. In the simulation, a pair of high-contrast and low-contrast 2-cm targets was located at 2.0-cm depth.

P_{high}/P_{low} versus source–detector separation for the pair of high- and low-contrast targets of 2.0-cm diameter located at 2.0-cm depth. The ratio P_{high}/P_{low} remains fairly constant over the entire range of source–detector separation. The mean value of P_{high}/P_{low} is 1.34, and the standard deviation is 0.57. Note that when the source–detector separation is larger, the total number of photons received at each detector is smaller, and the signal-to-noise ratio (SNR) is lower. The mean values and standard deviations of P_{high}/P_{low} under other imaging conditions are given in Table 2.

In Fig. 6, solid lines with circles show the average P_{high}/P_{low} versus target center depth for the three pairs of large (blue), medium (red), and small (black) targets. The average P_{high}/P_{low} values were 1.28, 1.34, 1.39, and 1.45 for the medium-size target located at 1.5-, 2.0-, 2.5-, and 3-cm depths, respectively, while the average values were 1.04, 1.14, 1.16, and 1.17 for the small 1-cm target located at the corresponding depths. On average, the larger, medium, and small high-contrast targets experience 1.64, 1.36, and 1.14 times higher light shadowing effect due to the target contrast compared with the low-contrast target of the same size. The results suggest that the 1-cm target is free of the posterior light shadowing effect. The ratio P_{high}/P_{low} is independent of the target location and depends on the target contrast only.

3.3 Image Reconstruction Results of the MC Simulations

The image reconstruction was performed on each data set, and the ratio of reconstructed maximum absorption coefficients of top and bottom target layers was calculated for each target location. In the reconstruction, the background region was divided into a relatively coarse mesh of pixel size 1.0×1.0 cm^2 in x and y dimensions, and the target region was segmented into a finer mesh of 0.1×0.1 cm^2 in x and y dimensions. The target region was chosen three to four times
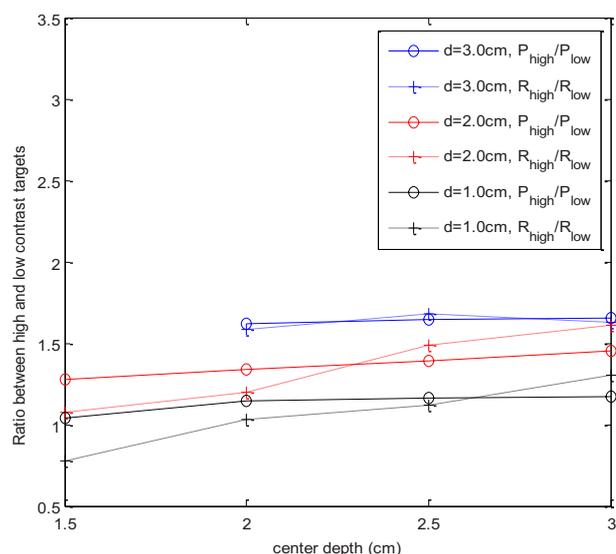
Fig. 6 Average ratio of P_{high}/P_{low} (intensity ratio) and $R_{high/low}$ (reconstruction ratio) versus target center location. The three groups of curves correspond to target diameter of 1 cm, 2 cm, and 3 cm. Both P_{high}/P_{low} and $R_{high/low}$ are independent of target location, as predicted by Eq. (8).

larger than the true target area. To compare the intensity ratio obtained from the MC simulation with the reconstructed maximum absorption ratio measured from the top and bottom target layers in depth, we have reconstructed targets in two layers. The first target layer was located at the center depth of the top half of the target, and the bottom target layer was located at the center depth of the bottom half of the target. The separation of two target layers was the radius of the target. This imaging reconstruction scheme matches the intensity ratio calculation used in simulation and makes the comparison easier.

The reconstruction results are listed in the second row of each category in Table 1. The reconstructed images are not shown here. The ratios of reconstructed maximum μ_a measured from the top-half target to the bottom-half target are listed in the third row of each category. For the high-contrast 3-cm target, the ratios were 3.30, 4.23, and 5.08 when the target was located at 2.0-, 2.5-, and 3.0-cm depth, respectively. For the low-contrast 3-cm target, the reconstructed ratios were 2.08, 2.52, and 3.13, respectively. Similarly, the ratio $R_{high/low}$, which is independent of the target location and depends only on the target contrast, is plotted in Fig. 6 using dashed lines with cross symbols. The ratio of $R_{high/low}$ closely follows the P_{high}/P_{low} computed from the MC simulations. The average ratios of $R_{high/low}$ for the three high- and low-contrast target pairs of larger, medium, and small were 1.63, 1.35, and 1.06.

3.4 Image Reconstruction Results of Phantom Experiments

Phantom experiments were performed at similar conditions as the simulation. The Intralipid solution was used to emulate typical breast tissue optical properties of $\mu_a=0.027$ cm^{-1} and $\mu_s'=7.20$ cm^{-1} calibrated at 780-nm wavelength. The high-contrast and low-contrast targets of three sizes were used to

emulate the small, medium, and large lesions of 1.0-, 2.0-, and 3-cm diameter. Each target was located at different depths from 1.5 cm to 3.0 cm with 0.5-cm increment in depth.

The reconstructed absorption maps were obtained following the same procedure described in Sec. 2.3. In the reconstruction, the coarse mesh was the same as the simulation in x and y spatial dimensions. The target region was segmented into a finer mesh of 0.25×0.25 cm^2 in x and y dimensions. The choice of fine-mesh size was based on considerations of the system signal-to-noise ratio and the total number of voxels with unknown optical proprieties. The layer or depth separation was chosen as 1.0 cm for coarse mesh and 0.5 cm for fine mesh, which were the same as those used in the clinical experiments. The fine-mesh target region was chosen three to four times larger than the true target area. In the reconstructed absorption map, each slice is the spatial x-y image of 8 cm $\times 8$ cm. The depth of each slice is marked in the figure. In order to compare with the clinical experiments, the reconstruction was performed in 0.5-cm spacing in depth. Thus, the 3-cm-diam target and the 2-cm-diam target occupied five target layers and three target layers, respectively. The other layers in depth were the background.

The reconstructed images of the 3-cm high-contrast target located at 2.0-, 2.5-, and 3-cm depth are shown in Figs. 7(a)–7(c), respectively. The images of the 3-cm low-contrast target located at the corresponding depths are shown in Figs. 8(a)–8(c), respectively. For each set of images, the measured maximum μ_a at the target layers are given in Table 3. If the ratios R of measured maximum μ_a obtained from the top target layer over that obtained from the second target layer are calculated, the ratio R depends on the target location and increases with the target depth, as predicted by Eq. (7).

The $R_{high/low}$ ratios for 1-cm targets that characterize the light shadowing effect due to contrast only were 0.97, 0.91, 0.97, and 0.99 for this pair of high- and low-contrast targets located at 1.5-, 2-, 2.5-, and 3-cm depths. The ratio $R_{high/low}$ was computed using R_{high} and R_{low} obtained from the first target layer over the second target layer. Compared with the simulation, the $R_{high/low}$ increases slightly with the target depth. When the target depth increases beyond 2.5 cm, the source–detector pairs greater than 5 to 6-cm separation mainly receive photons from the bottom layers and the signal-to-noise ratios of these data are lower compared with those obtained from shorter pairs. This problem is more pronounced when a larger absorber is embedded in the medium. As a result, the reconstructed maximum μ_a values at the bottom layers were slightly above the background values and were the same for both high- and low-contrast targets. Under this condition, the $R_{high/low}$ is mainly the ratio of reconstructed maximum μ_a values of high- and low-contrast targets at the top layer, and it is higher than that predicted by Eq. (8). However, the mean value is 1.54, which is very close to the mean value of 1.6 obtained from the MC simulation. Thus, on average, the larger high-contrast target of 3 cm in size has experienced 1.6 times higher light shadowing effect due to the target contrast compared with the low-contrast target of the
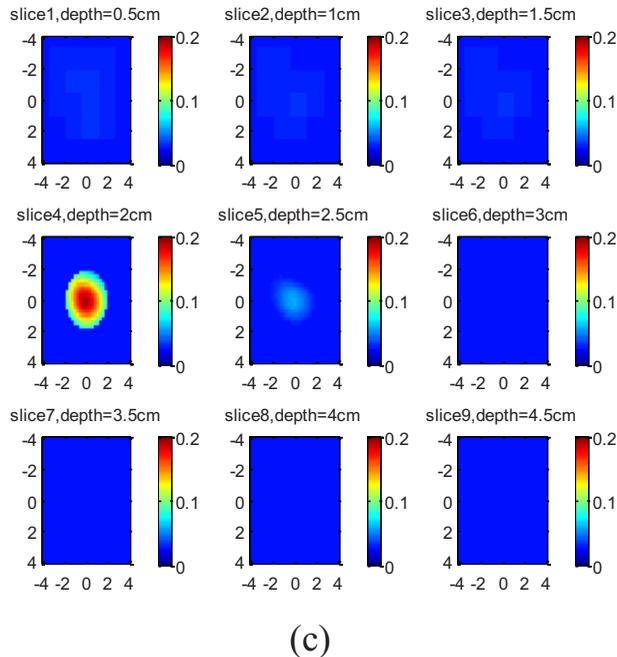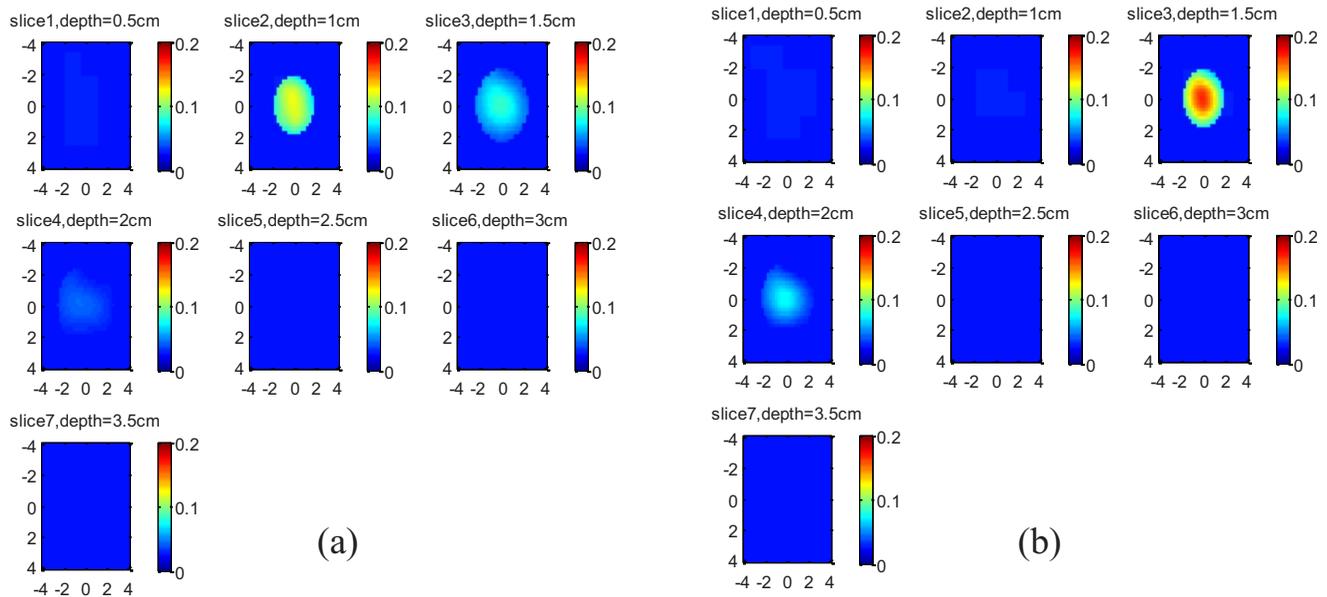
(a)

(b)

(c)

Fig. 7 Experimental results of 3-cm-diam high-contrast target. The target center was located at (a) 2.0 cm, (b) 2.5 cm, and (c) 3.0 cm, respectively. Each slice is the tomographic display of reconstructed absorption distribution in 8 cm×8 cm spatial x-y dimensions. The depth of each slice is marked in the figure.

same size.

For the 1-cm target, the reconstructed images of the high-contrast target located at 1.5, 2, 2.5, and 3 cm are shown in Figs. 9(a)–9(d), respectively, and the images of the low-contrast target located at the corresponding depths are shown in Figs. 10(a)–10(d), respectively. For each set of images, the measured maximum μ_a at target layers is given in Table 3. The ratio R depends on the target location and slightly increases with the target depth.

Note that in our reconstruction procedure with 0.5-cm increment in depth, the small target with diameter of 1 cm is typically reconstructed in one target layer. However, to compare results obtained from large and medium-size targets, the small targets were reconstructed in two target layers with the top layer located at the middle of the top-half of the target and the bottom layer located at the middle of the bottom-half of the target.

The $R_{high/low}$ ratios for 1-cm targets that characterize the light shadowing effect due to contrast only were 0.97, 0.91, 0.97, and 0.99 for this pair of high- and low-contrast targets located at 1.5-, 2-, 2.5-, and 3-cm depths. These values were constant over the target depths studied. This result indicates
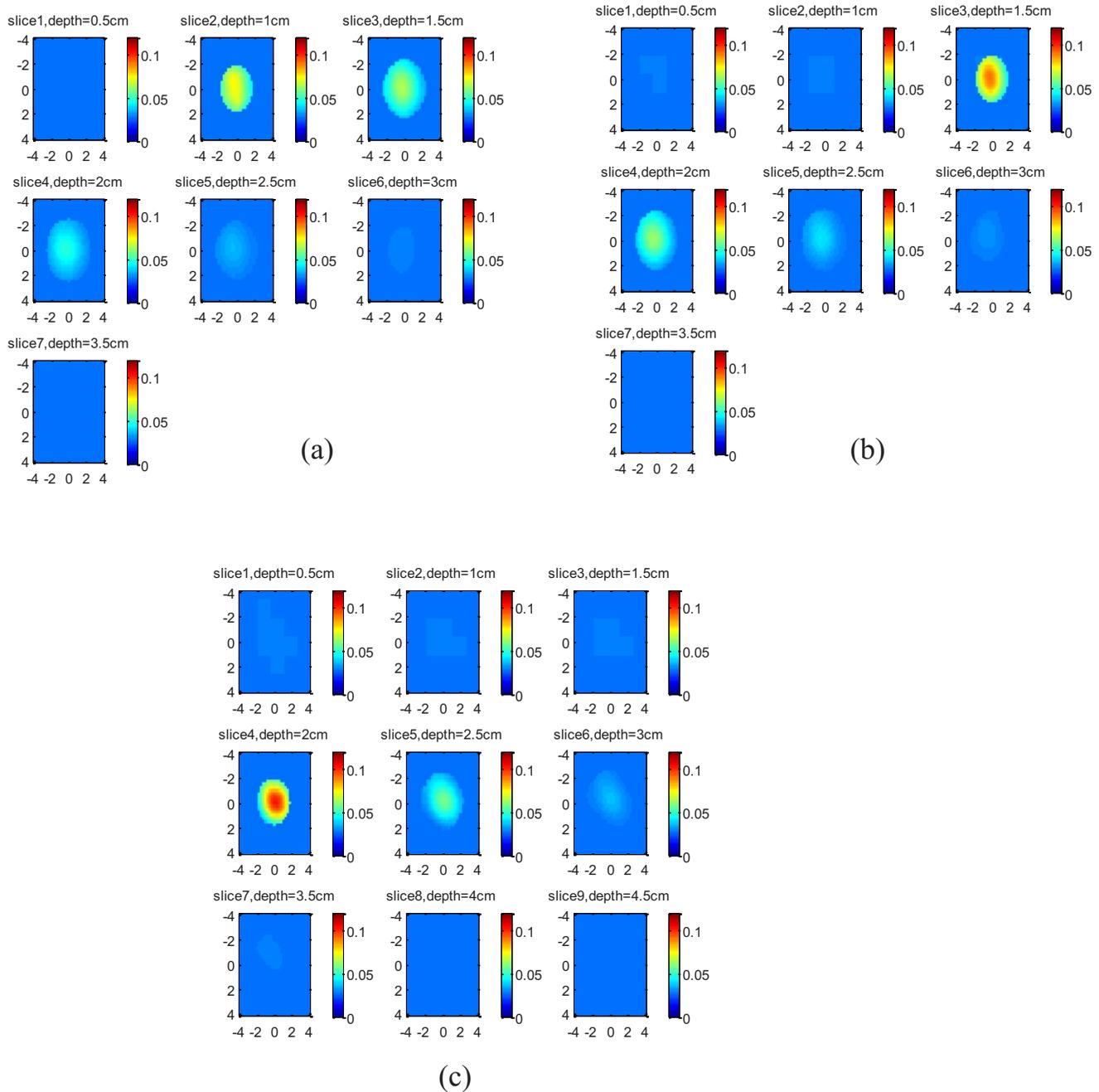
(a)

(b)

(c)

Fig. 8 Experimental results of 3-cm-diam low-contrast target. The target center was located at (a) 2.0 cm, (b) 2.5 cm, and (c) 3.0 cm, respectively. Each slice is the spatial *x-y* image of 8 cm×8 cm, and the depth of each slice is marked in the figure.

that on average, the small high-contrast target of 1 cm in size did not experience the light shadowing effect due to target optical contrast.

The phantom experiments were also performed on the medium-size 2-cm diameter high- and low-contrast targets. The reconstruction results are given in Table 3, and the reconstructed images are not shown here. The $R_{high/low}$ ratios for the 2-cm target, which characterize the light shadowing effect due to contrast only, were 1.00, 1.20, 1.25, and 1.39 for this pair of high- and low-contrast targets located at 1.5-, 2-, 2.5-, and 3-cm depths. The ratio $R_{high/low}$ was computed using R_{high} and R_{low} obtained from the first target layer over that obtained

from the second target layer. The $R_{high/low}$ increases slightly with the target depth for the same reason discussed earlier. However, the mean value, 1.22, is very close to the mean value of 1.36 obtained from the MC simulation.

Figure 11 shows the $R_{high/low}$ versus target depth obtained from 1.0-, 2.0-, and 3.0-cm diameter targets. The $R_{high/low}$ was computed using R_{high} and R_{low} obtained from the first target layer over the second target layer. The $R_{high/low}$ is fairly constant over the depth studied; however, it increases slightly at deeper depth for the medium and larger target data because the signal-to-noise ratio decreases with depth.

Table 3 Reconstruction results for phantom experiments.

		Center Depth (cm)							
		1.5 cm		2.0 cm		2.5 cm		3.0 cm	
Target Diameter (cm)		High-Contrast Target	Low-Contrast Target	High-Contrast Target	Low-Contrast Target	High-Contrast Target	Low-Contrast Target	High-Contrast Target	Low-Contrast Target
$D = 1.0$ cm	Reconstructed maximum μ_a (cm^{-1}) [max in top layer; max in bottom layer]	0.155 0.172	0.086 0.093	0.161 0.183	0.084 0.087	0.155 0.169	0.075 0.079	0.165 0.171	0.080 0.083
$D = 2.0$ cm	Reconstructed maximum μ_a (cm^{-1}) [max in first layer; max in second layer; max in third layer]	0.120 0.089 0.052	0.109 0.081 0.046	0.160 0.074 0.030	0.129 0.071 0.028	0.144 0.064 0.031	0.121 0.067 0.040	0.139 0.069 0.040	0.093 0.064 0.045
$D = 3.0$ cm	Reconstructed maximum μ_a (cm^{-1}) [max in first layer; max in second layer; max in third layer; max in fourth layer; max in fifth layer]			0.120 0.084 0.044 0.028 0.028	0.074 0.065 0.048 0.030 0.028	0.167 0.075 0.028 0.028 0.028	0.090 0.061 0.040 0.031 0.028	0.189 0.057 0.028 0.028 0.028	0.100 0.057 0.035 0.022 0.028

3.5 Clinical Examples

Two examples were obtained from our ongoing clinical study conducted at the University of Connecticut Health Center. Figure 12(a) shows a co-registered ultrasound B-scan of a suspicious lesion. The center of the lesion was located at 2.75-cm depth, and the size of the lesion was about 2.7 cm. The fitted background tissue optical properties were μ_a =0.031 cm^{-1} and μ_s' =3.10 cm^{-1} at 780 nm. Using the same reconstruction scheme as the phantom experiment, the lesion was reconstructed with a 0.5-cm increment, and the depth of each slice is marked in the figure. Considering the higher noise level in clinical data, the target region was segmented into a fine mesh of voxel size $0.5 \times 0.5 \times 0.5$ cm^3 and the coarse mesh of $1.0 \times 1.0 \times 1.0$ cm^3. The fine-mesh region chosen was 4.5 times larger than the target area estimated by ultrasound. The reconstructed absorption map is shown in Fig. 12(b). At the first target layer, the reconstructed maximum μ_a was 0.244 cm^{-1}, the next layer was 0.116 cm^{-1}, and the last layer was only 0.041 cm^{-1}. The ratio between the first and second layer was 2.11. Ultrasound-guided core biopsy revealed that the lesion was an invasive lobular carcinoma.

Figure 13(a) shows a co-registered ultrasound B-scan of a suspicious lesion. The lesion center was located at 1.8-cm depth, and the diameter of the lesion was about 3.0 cm. The fitted tissue background optical properties were μ_a =0.012 cm^{-1} and μ_s' =3.16 cm^{-1} at 780 nm. The lesion was reconstructed with a 0.5-cm increment, and the reconstructed absorption map is shown in Fig. 13(b). In this example, the reconstructed maximum μ_a was 0.087 cm^{-1} at the first target layer and 0.068 cm^{-1} and 0.049 cm^{-1} at the second and third target layers, respectively. The ratio between the first layer

and the second layer was 1.28, and the ratio between the first layer and the third layer was 1.77. Ultrasound-guided core biopsy revealed that the lesion was a benign mass with fibrocystic changes.

The $R_{high/low}$ due to optical contrast only for this pair of malignant and benign lesions of 3-cm size is 1.6. It is interesting to note that the location and size of this pair of malignant and benign lesions are slightly different; however, the ratio $R_{high/low}$ is very close to that obtained from the pair of 3-cm high- and low-contrast phantom targets. This result is promising and suggests that it is possible to use the simple measure $R_{high/low}$ derived from this paper to compare the malignant versus benign lesions.

4 Discussion and Summary

In our clinical data obtained from large cancers, we have observed two major types of vascular distribution patterns: heterogeneous distribution in both spatial and depth dimensions, and homogeneous distribution in spatial dimensions only and significant posterior light shadowing effect in depth.[19] Heterogeneous vascular distributions are often seen in advanced large cancers of more than 3 cm in size.[15] This paper has systemically characterized and quantified the posterior light shadowing effect. In this paper, we derived a simple measure to assess the light shadowing effect caused by the optical contrast only. Because of the depth-dependent weight distribution of the diffusive waves, the ratio of reconstructed μ_a measured from the top target layer to the deeper target layers depends on the target depth. The posterior shadowing effect caused by highly absorbing malignant lesions can be separated from the depth-dependent reconstruction using the
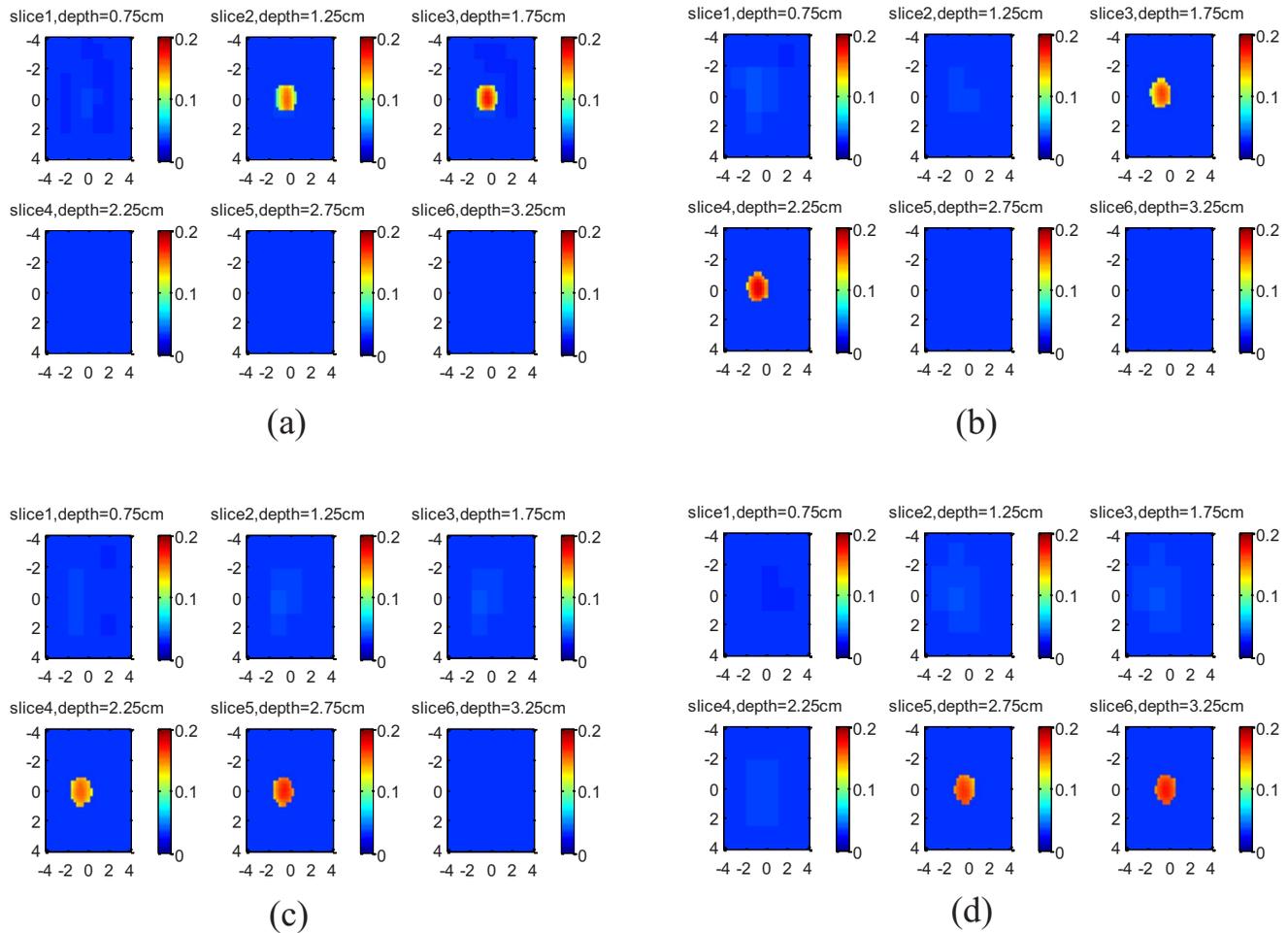
Fig. 9 Experimental results of 1-cm-diam high-contrast target. From (a) to (d), the target center was located at 1.5 cm, 2.0 cm, 2.5 cm, and 3.0 cm, respectively. Each slice is the spatial *x*-*y* image of 8 cm×8 cm, and the depth of each slice is marked in the figure.

simple measure derived from this paper. The measure is obtained from a pair of high- and low-contrast targets of a similar size, a similar target location, and similar background optical properties, and it is independent of target depth. To apply this measure to clinical diagnosis, we will need to evaluate several groups of malignant and benign lesions. Each group of malignant and benign lesions will have a similar size and be located at a similar depth. The background optical properties should be similar as well. The ratio $R_{high/low}$ of each group will be computed to validate the phantom results, and initial observations from clinical cases indicate that it is independent of depth and depends on target contrast only. With further clinical validation, we may be able to diagnose malignant versus benign lesions of a subpopulation of patients who present posterior light shadowing effect, based on the ratio of maximum μ_a measured from an absorption map at the first and second target layers. If this ratio is higher than a certain threshold compared with that obtained from the typical large benign lesions of similar size located at similar depth, the chance of the lesion being a malignant cancer is higher. We anticipate that this light shadowing effect due to optical contrast only can be used to further diagnose larger cancers versus benign lesions in addition to quantitative optical contrast. For small lesions of approximately 1 cm in size, the light

shadowing effect is negligible, and the diagnosis should be based on quantitative optical contrast only.

The diagnostic value of optical tomography is to distinguish benign from malignant lesions. Large benign lesions, especially some fibroadenomas and fibrocystic lesions, also present posterior light shadowing, as shown in this study. To quantify how much light shadowing effect is present in malignant lesions as compared with benign lesions, we will need to use benign lesions as references to cancel out the depth-dependent light shadowing effect. As seen from the clinical examples, the lesions may not have exact spherical shape. We have used the ratio of maximum μ_a reconstructed from the top two layers to estimate the R_{high} and R_{low}. In addition, the lesion sizes, locations and background optical properties may not be exactly the same. The ratio $R_{high/low}$ obtained from the two clinical examples was very close to that obtained from the paired high- and low-contrast phantom targets of a similar size. The accuracy and robustness of using this simple measure, $R_{high/low}$, is yet to be demonstrated in a large patient pool presenting posterior light shadowing effect.

The limitation of this study is that only three target sizes were studied, which covered the majority of the lesions we have seen in the clinical studies, but not all. As discussed
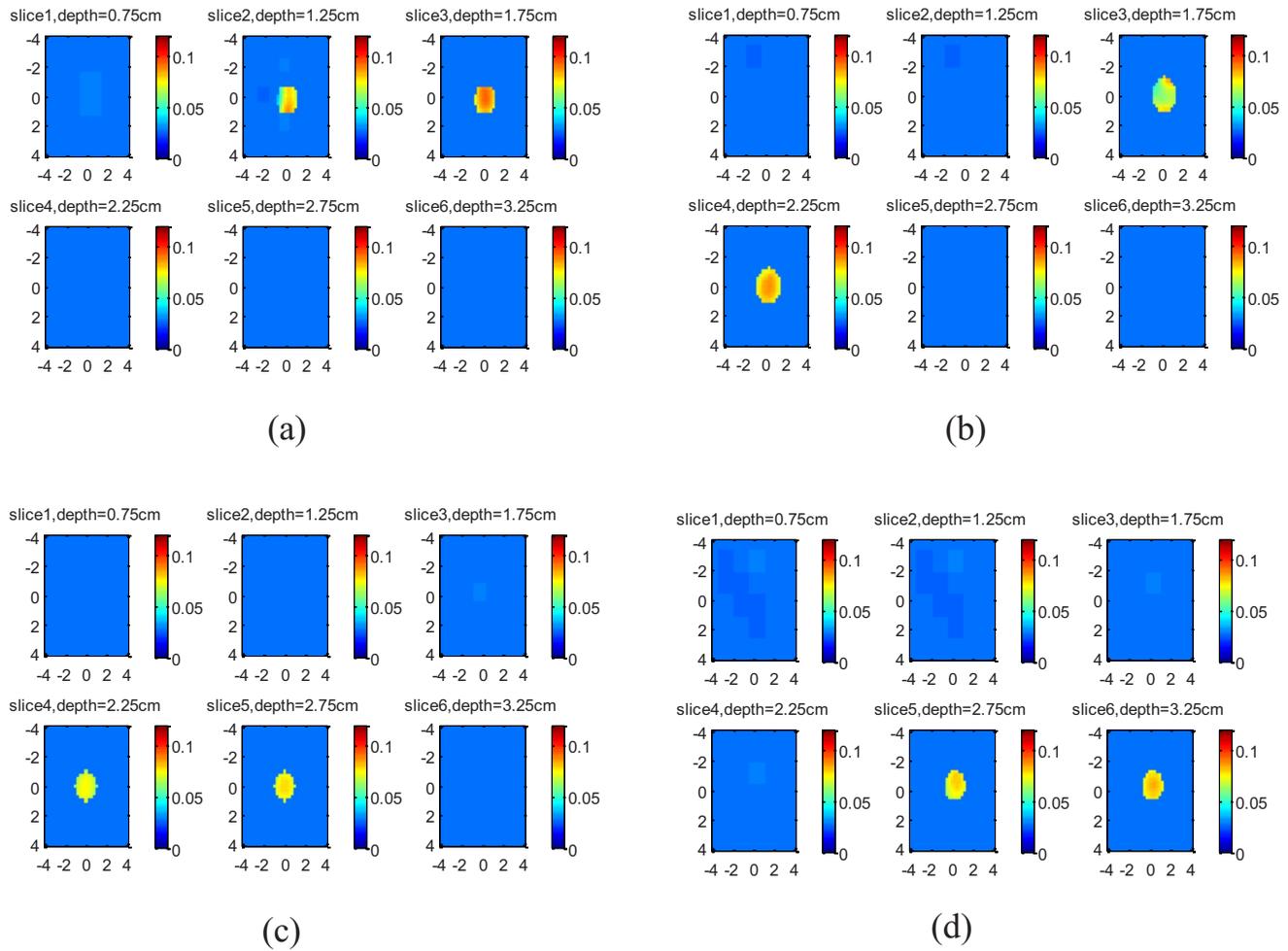
Fig. 10 Experimental results of 1-cm-diam low-contrast target. The target center was located at (a) 1.5 cm, (b) 2.0 cm, (c) 2.5 cm, and (d) 3.0 cm, respectively. The depth of each slice is marked in the figure.

earlier, advanced cancers of more than 3 cm in size often present heterogeneous vascular distributions that can be used to diagnose the malignance in addition to the light shadowing effect reported here.[19]

In our imaging reconstruction, the linear Born approximation is used to compute the weight matrix, which is independent of target contrast. Thus, the κ in Eq. (7) can be cancelled out for a pair of high- and low-contrast targets of a similar size located at a similar depth and embedded in a similar background medium. For large high-contrast absorbers, the Born approximation is not accurate. Therefore, the κ may weakly depend on the target contrast as well. However, the reasonably good agreement of our reconstruction results with MC photon-tracking results suggests that the simple measure derived in the paper can be used as a first-order approximation for the target sizes evaluated.

This paper to the best of our knowledge reports the first study of the light shadowing effect due to optical contrast. The simple measure derived in the paper may be useful to provide important guidelines to imagers in diagnosing larger malignant cancers versus benign lesions once it is further validated by a larger group of patients.
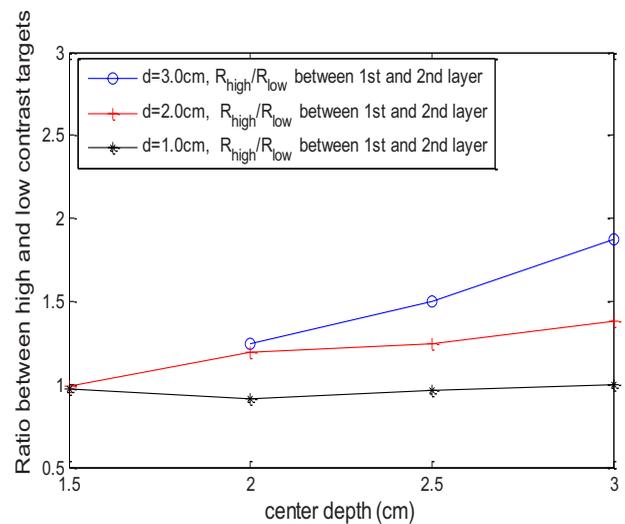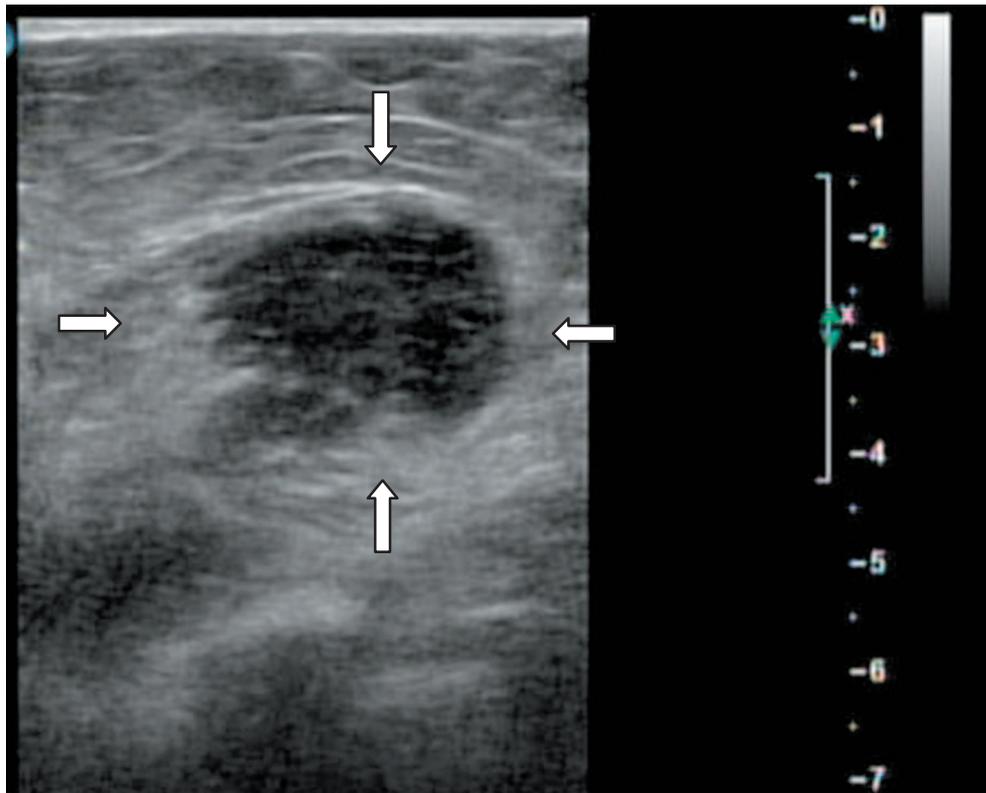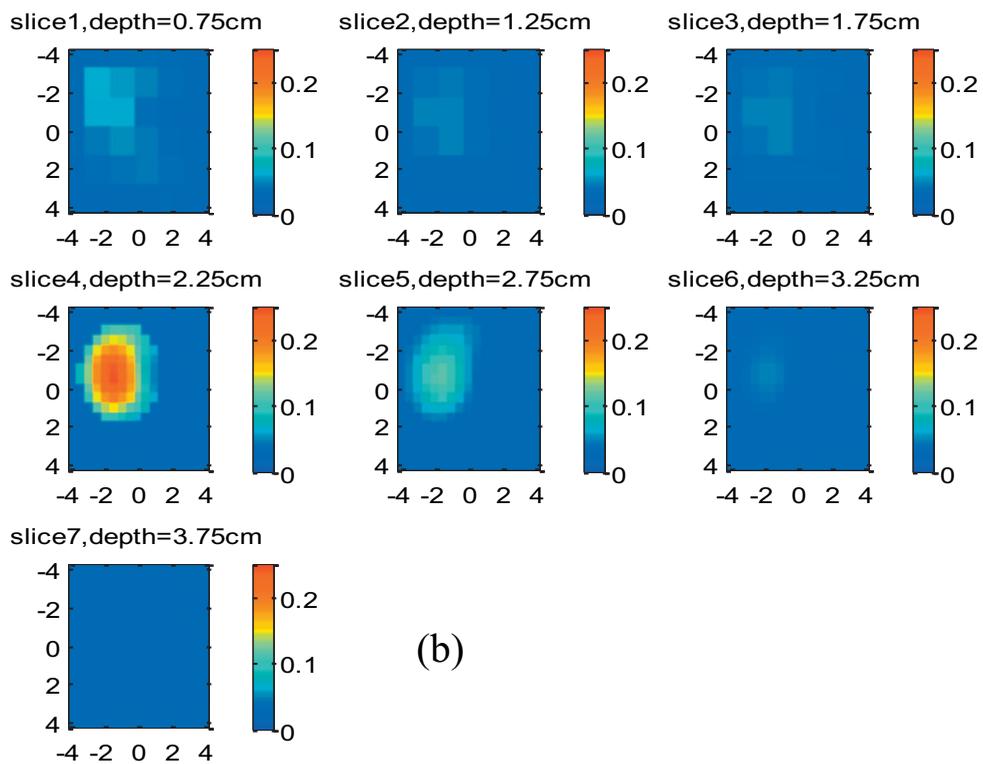

Fig. 11 The ratio $R_{high/low}$ versus target center location obtained from phantom experiments. The solid lines are the ratios computed using R_{high} and R_{low} obtained from the first target layer over the second target layer.
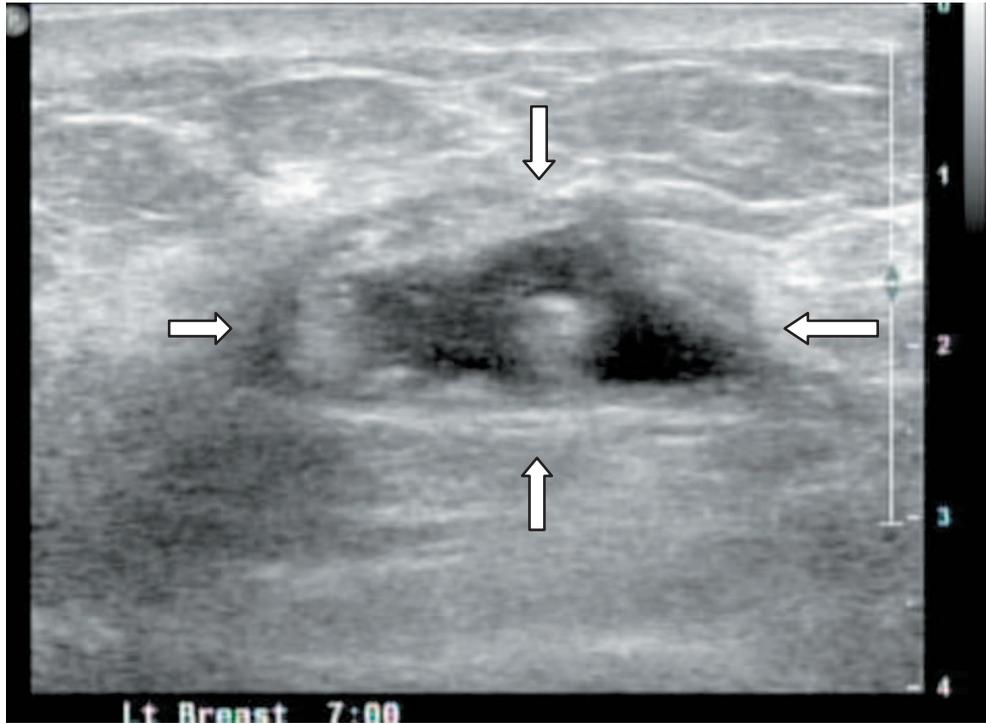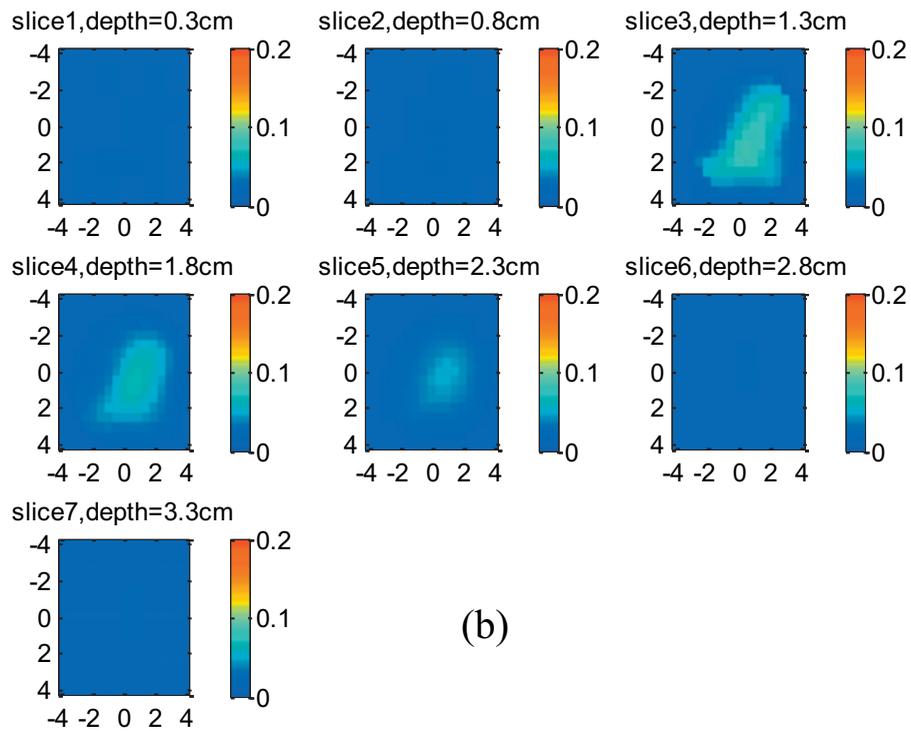
(a)

(b)

Fig. 12 An example of a 2.7-cm malignant lesion. (a) A co-registered ultrasound B-scan image of the cancer. (b) Reconstructed absorption map at 780 nm.

(a)

(b)

Fig. 13 An example of a 3-cm benign lesion. (a) A co-registered ultrasound B-scan image of the lesion. (b) Reconstructed absorption maps at 780 nm.

References

1. A. Yodh and B. Chance, "Spectroscopy and imaging with diffusing light," *Phys. Today* **48**(3), 34–40 (1995).
2. B. Tromberg, N. Shah, R. Lanning, A. Cerussi, J. Espinoza, T. Pham, L. Svaasand, and J. Butler, "Non-invasive *in vivo* characterization of breast tumors using photon migration spectroscopy," *Neoplasia* **2**(1:2), 26–40 (2000).
3. B. Chance, S. Nioka, J. Zhang, E. Conant, E. Hwang, S. Briest, S. Orel, M. Schnall, and B. Czerniecki, "Breast cancer detection based on incremental biochemical and physiological properties of breast cancers: a six-year, two-site study," *Acad. Radiol.* **12**(8), 925–933 (2005).
4. S. Poplack, T. Tosteson, W. Wells, B. Pogue, P. Meaney, A. Hartov, C. Kogel, S. Soho, J. Gibson, and K. Paulsen, "Electromagnetic breast imaging: results of a pilot study in women with abnormal mammograms," *Radiology* **243**(2), 350–359 (2007).
5. D. Grosenick, K. Moesta, H. Wabnitz, J. Mucke, C. Stroszczynski, R. Macdonald, P. Schlg, and H. Rinneberg, "Time-domain optical mammography: initial clinical results on detection and characterization of breast tumors," *Appl. Opt.* **42**(16), 3170–3186 (2003).
6. L. Spinelli, A. Torricelli, A. Pifferi, P. Taroni, G. Danesini, and R. Cubeddu, "Characterization of female breast lesions from multi-wavelength time-resolved optical mammography," *Phys. Med. Biol.* **50**(11), 2489–2502 (2005).
7. R. Choe, A. Corlu, K. Lee, T. Durduran, S. Konecky, M. Grosicka-Koptyra, S. Arridge, B. Czerniecki, D. Fraker, A. DeMichele, B. Chance, M. Rosen, and A. Yodh, "Diffuse optical tomography of breast cancer during neoadjuvant chemotherapy: a case study with comparison to MRI," *Med. Phys.* **32**(4), 1128–1139 (2005).
8. E. Heffer, V. Pera, O. Schutz, H. Siebold, and S. Fantini, "Near-infrared imaging of the human breast: complementing hemoglobin concentration maps with oxygenation images," *J. Biomed. Opt.* **9**(6), 1152–1160 (2004).
9. X. Gu, Q. Zhang, M. Bartlett, L. Schutz, L. Fajardo, and H. Jiang, "Differentiation of cysts from solid tumors in the breast with diffuse optical tomography," *Acad. Radiol.* **11**(1), 53–60 (2004).
10. B. J. Tromberg, A. Cerussi, N. Shah, M. Compton, A. Durkin, D. Hsiang, J. Butler, and R. Mehta, "Diffuse optics in breast cancer: detecting tumors in pre-menopausal women and monitoring neoadjuvant chemotherapy," *Breast Cancer Res. Treat.* **7**, 279–285 (2005).
11. A. Cerussi, D. Hsiang, N. Shah, R. Mehta, A. Durkin, J. Butler, and B. J. Tromberg, "Predicting response to breast cancer neoadjuvant chemotherapy using diffuse optical spectroscopy," *Proc. Natl. Acad. Sci. U.S.A.* **104**, 4014–4019 (2007).
12. Q. Zhu, N. Chen, and S. Kurtzman, "Imaging tumor angiogenesis using combined near infrared diffusive light and ultrasound," *Opt. Lett.* **28**(5), 337–339 (2003).
13. Q. Zhu, M. Huang, N. Chen, K. Zarfos, B. Jagjivan, M. Kane, P. Hegde, and S. Kurtzman, "Ultrasound-guided optical tomographic imaging of malignant and benign breast lesions: initial clinical results of 19 cases," *Neoplasia* **5**(5), 379–388 (2003).
14. Q. Zhu, E. B. Cronin, A. A. Currier, H. S. Vine, M. Huang, N. Chen, and C. Xu, "Benign versus malignant breast masses: optical differentiation with U.S.-guided optical imaging reconstruction," *Radiology* **237**, 57–66 (2005).
15. Q. Zhu, S. H. Kurtzman, P. Hegde, S. Tannenbaum, M. Kane, M. Huang, N. G. Chen, B. Jagjivan, and K. Zarfos, "Utilizing optical tomography with ultrasound localization to image heterogeneous hemoglobin distribution in large breast cancers," *Neoplasia* **7**, 263–270 (2005).
16. Q. Zhu, S. Tannenbaum, P. Hedge, C. Xu, and S. Kurtzman, "Non-invasive monitoring of breast cancer during neoadjuvant chemotherapy using optical tomography with ultrasound localization: a pilot study," *Neoplasia* **10**(10), 1028–1040 (2008).
17. B. Pogue, T. McBride, S. Osterman, S. Poplack, U. Osterberg, and K. Paulsen, "Quantitative hemoglobin tomography diffuse near-infrared spectroscopy: pilot results in the breast," *Radiology* **218**, 261–266 (2001).
18. S. Jiang, B. Pogue, C. Carpenter, S. Poplack, W. Wells, C. Kogel, J. Forero, L. Muffly, G. Schwartz, K. Paulsen, and P. Kaufman, "Evaluation of breast tumor response to neoadjuvant chemotherapy with tomographic diffuse optical spectroscopy: case studies of tumor region-of-interest changes," *Radiology* **252**, 551–560 (2009).
19. Q. Zhu, P. Hegde, A. Ricci, Jr., M. Kane, E. Cronin, Y. Ardeshirpour, C. Xu, A. Aguirre, S. Kurtzman, P. Deckers, and S. Tannenbaum, "The potential role of optical tomography with ultrasound localization in assisting ultrasound diagnosis of early-stage invasive breast cancers," *Radiology* (in press).
20. Y. Xu and Q. Zhu, "Imaging heterogeneous absorption distribution of advanced breast cancers using optical tomography guided by ultrasound," *Biomedical Optics (BIOMED)* 2010 paper: BSuD92, OSA Technical Digest (CD).
21. M. Huang and Q. Zhu, "Dual-mesh optical tomography reconstruction method with a depth correction that uses *a priori* ultrasound information," *Appl. Opt.* **43**(8), 1654–1662 (2004).
22. L. Wang, S. L. Jacques, and L. Zheng, "MCML-Monte Carlo modeling of light transport in multi-layered tissues," *Comput. Methods Programs Biomed.* **47**, 131–146 (1995).
23. M. Das, C. Xu, and Q. Zhu, "Analytical solution for light propagation in a two-layer tissue structure with a tilted interface for breast imaging," *Appl. Opt.* **45**(20), 5027–5036 (2006).
24. C. Xu., B. Yuan, and Q. Zhu, "Optimal probe design for breast imaging using near-infrared diffused light," *J. Biomed. Opt.* **13**(4), 044002 (2008).
25. E. Hecht, *Optics*, 2nd ed., Addison-Wesley, New York (1987).
26. C. Xu and Q. Zhu, "Reference selection of NIR breast imaging using perturbation approach," in *Progress in Biomedical Optics and Imaging - Proceedings of SPIE*, Optical Tomography and Spectroscopy of Tissue VII, B. Chance, R. R. Alfano, B. J. Tromberg, M. Tamura, and E. M. Sevick-Muraca, Eds., Vol. **6434**, pp. 643415.1–15 (2007).
27. Q. Zhu, C. Xu, P. Guo, A. Aguirre, B. Yuan, F. Huang, D. Castilo, J. Gamelin, S. Tannenbaum, M. Kane, P. Hegde, and S. Kurtzman, "Optimal probing of optical contrast of breast lesions of different size located at different depths by U.S. localization," *Technol. Cancer Res. Treat.* **5**(4), 365–380 (2006).